CHAPTER VI

LIGHT SCATTERING STUDIES OF INTERSTELLAR DUST ANALOGUE GRAPHITE AND FAYALITE MIXTURE

6.1 Introduction

Extinction and scattering properties of dust present in line of sight between observer and source must be interpreted properly in order to reveal original spectrum of light sources [1-3]. The determination of shape, size and composition of interstellar dust grains found in different extraterrestrial environments is difficult because of its dependence on direction of observations [4, 5]. The collection of real dust particles present in extraterrestrial environments is not possible in most of the cases with a few exceptions like the onboard spectrometers and in situ dust detectors of Ulysses, Cassini, Galileo and Helios spacecraft's [6, 7]. This problem can be simplified by laboratory production of dust analogue samples and carrying out simulations with various models [8].

Along with acting as the natural scatterer for all observed light sources the amorphous graphite and silicate dust grains together play a vital role in the formation of H_2, H_2O, CO, CO_2, CH_3OH, and CH_4 in the interstellar medium as observed in some prominent absorption bands for e.g. 2175 cm^{-1} and in the 2.5-30 μm range [9-15]. These two components of dust must be studied in the visible to IR range with models to fit observed scattering curves and absorption bands. Graphite is a major component of the cosmic dust clouds [16]. While silicates are abundant in the interstellar medium along with meteorites with higher probabilities than graphite and PAHs [17, 18]. Some well accepted simulation tools are also available to dust models in a broad wavelength range from UV-IR e.g. SKIRT [19]. An efficient dust model must include all possible physical parameters of the scatterer considering diverse properties of dust in different environments [20].

This chapter provides a detailed description of the light scattering studies with mixtures of graphite and fayalite as interstellar dust analogues. The study is performed using two computational models in the visible wavelength region. A comparative analysis of the theoretical and experimental results of shape and size averaged phase function and degree of linear polarization are done to validate the models.

6.2 Computational dust models of graphite and fayalite

Six target geometries were generated based on the random Gaussian (Figure 6.1 and 6.2) shapes suggested by Zubko et al. and Nousiainen and Muinonen [21, 22]. The aspect ratios for all the shapes are fixed between 2 and 3. Two models are developed based on these shapes Model1 and Model2. While converting these shapes into dipoles the distance between two adjacent dipoles are flexible so as to fit in target geometries of different shape and sizes. The number of dipoles used for the two models are fixed at 50k and 100k respectively.

A number of nonconventional variables are used in the models to make it more realistic. These are elemental composition of graphite and fayalite, number of orientation directions, number of dipoles along with the particle size distribution and refractive indices. Among the parameters the alignment of dust particles is the most difficult parameter to consider while modeling.

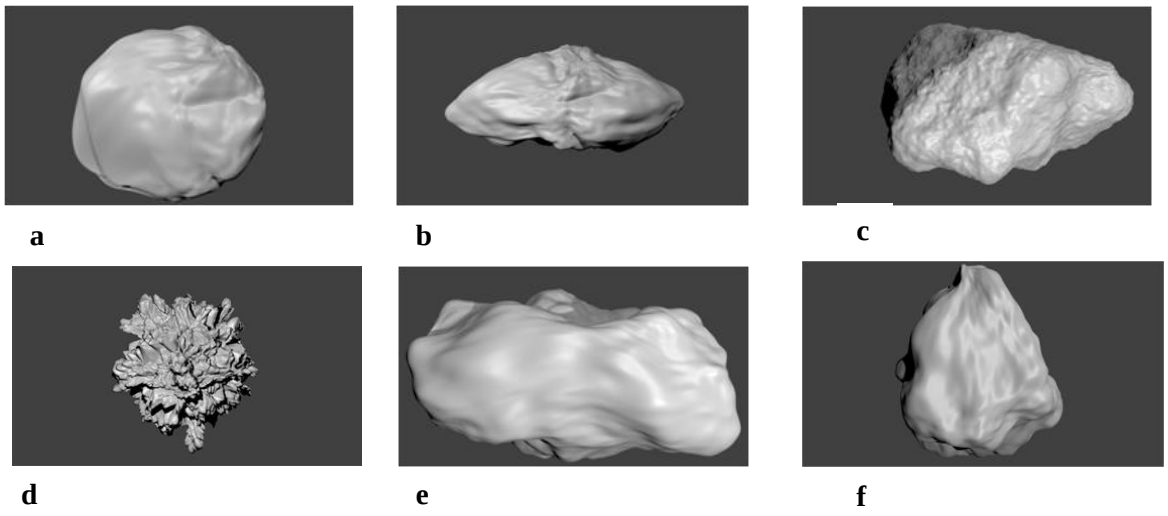

Figure 6.1 (a), (b), (c), (d), (e) and (f), Blender representation of target geometries shape1, shape2, shape3, shape4, shape5 and shape6 used in the models.

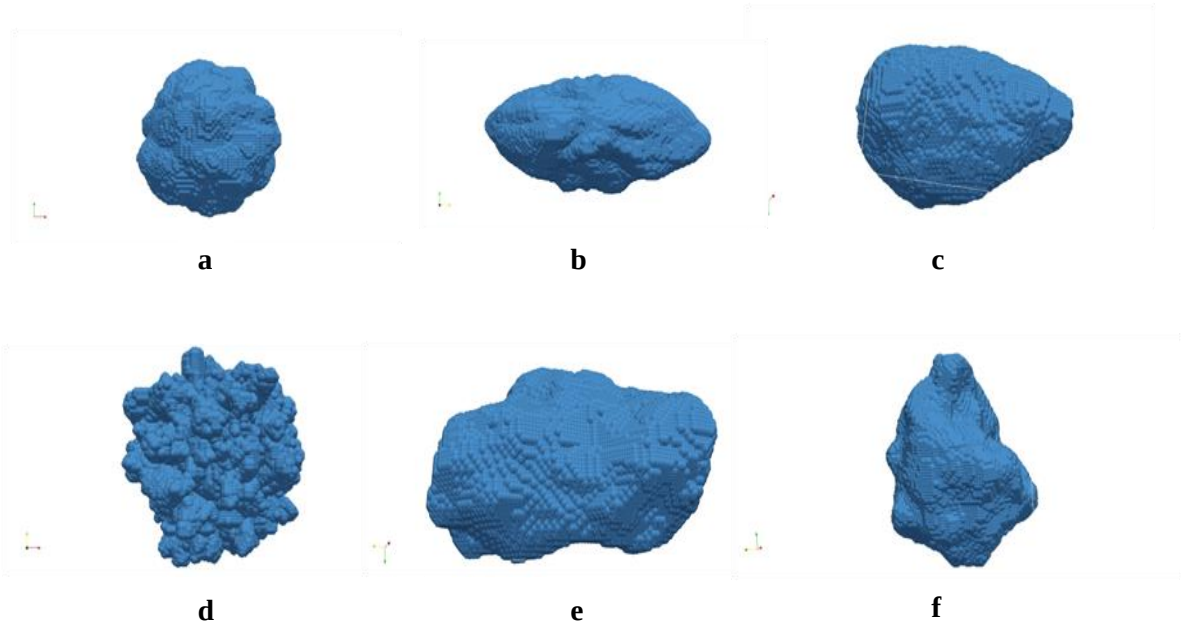

Figure 6.2 (a), (b), (c), (d), (e) and (f), 3d rendered dipole representation of the target geometries.

In all the computations the DDA condition [23, 24] is fulfilled for most of the cases. A table (Table 6.1) is provided in which the particle sizes are given for each of the wavelengths up to which the $|m|kd$ criterion is satisfied.

Table 6.1 Maximum particle sizes at which the $|m|kd \leq 1$ condition is satisfied.

Sample	Wavelength	Particle size at 50k dipoles	Particle size at 100k dipoles
Graphite	543.5 nm	1.0 µm	1.2 µm
	594.5 nm	1.1 µm	1.3 µm
	632.8 nm	1.2 µm	1.5 µm
Fayalite	543.5 nm	1.3 µm	1.6 µm
	594.5 nm	1.4 µm	1.6 µm
	632.8 nm	1.5 µm	1.8 µm

We have taken all possible measures within our capability to ensure higher accuracies in the calculations of orientation directions. The only drawback is that due to inadequate computational resources the number of orientation directions considered for averaging are limited. The measurements are performed in accordance with the random orientation conditions i.e. performed over a long duration of time and the system is assumed to be ergodic. When these conditions are satisfied the averaging over orientations direction for complete random orientation can be performed, where time averaging can be replaced by ensemble averaging over orientation directions [25, 26].

Again the scattering system is defined by two coordinate systems – one the Laboratory frame and another the target frame. One is dynamic with respect to the other with a common origin**.** This is another important condition for random orientation averaging [25-27]. In DDSCAT the laboratory frame is defined in such a way that the incident beam propagates in the $+x$ direction. And the target is specified by two orthogonal unit vectors $\hat{a}_1$ and $\hat{a}_2$ assumed to be frozen in the target. The resultant target frame can be defined by using three unit vectors $\hat{a}_1, \hat{a}_2$ and $\hat{a}_3$, where $\hat{a}_3 = \hat{a}_1 \times \hat{a}_2$. Further three angles are used to represent the target orientations which are θ, ϕ and β. θ and ϕ represents the direction of $\hat{a}_1$ relative to incident beam. While β represents the rotation of target around $\hat{a}_1$ axis.

For randomly oriented targets the scattering matrix elements can be measured as [28],

$$\langle F \rangle = \frac{1}{8\pi^2} \int_0^{2\pi} d\beta \int_{-1}^{1} d\cos\theta \int_0^{2\pi} d\phi F(\beta, \theta, \phi) \qquad \textbf{6.1}$$

Now the random orientational averaging is achieved by running β and ϕ from 0^0 to 360^0 and θ from 0^0 to 180^0 [28].

It has been proved that to achieve complete random orientation a large number of orientation directions must be used in the DDA computations [29, 30]. But due to our restrictions in available computational resources we are forced to restrict the number of orientations to lower values. Also our aim is to study only the combined effect of various modelling variables on the scattering properties of dust particles. In order to develop highly accurate dust models a sufficiently higher number of dipoles are required (not applicable in this case). This might result in some inaccuracies in the computed parameters.

6.3 Physical properties of the graphite and fayalite particles

The graphite samples are collected from Sigma Aldrich, while the fayalite microparticles (Fe_2SiO_4) are synthesized in the laboratory using a chemical route as suggested by De Angelis [31, 32]. In a particle sprayer or nebulizer (fitted in the setup) the fayalite and graphite microparticles are mixed in a 1:1 ratio. But after the samples are sprayed into the scattering volume, due to the probability distribution effects this ratio will not remain same during a particular scattering event. The Scanning electron micrography (SEM) analyses reveal highly irregular shapes of both graphite and fayalite samples (Figure 6.3). It also provides visual evidences of the particle size distribution and surface roughness. But it's not possible to consider each and every shape along with all the particle sizes considering the high irregularity and dispersions. Therefore it is reasonable to select a few shapes of interest which is supposed to resemble majority of the sample in both cases. The particle size distribution used is a lognormal function (Figure 4) with modal radius (r_m) = 1 μm, size ranges (r) = 0.3 to 5 μm, and standard deviation (σ) = 1.5. [31, 33],

$$\frac{dn}{d\ln(r)} = \frac{N_d}{\sqrt{2\pi}\ln\sigma}\exp\left[-\frac{(\ln r - \ln r_m)^2}{2(\ln\sigma)^2}\right] \qquad \textbf{6.2}$$

where 'N' is the number of particles with modal radius r_m .

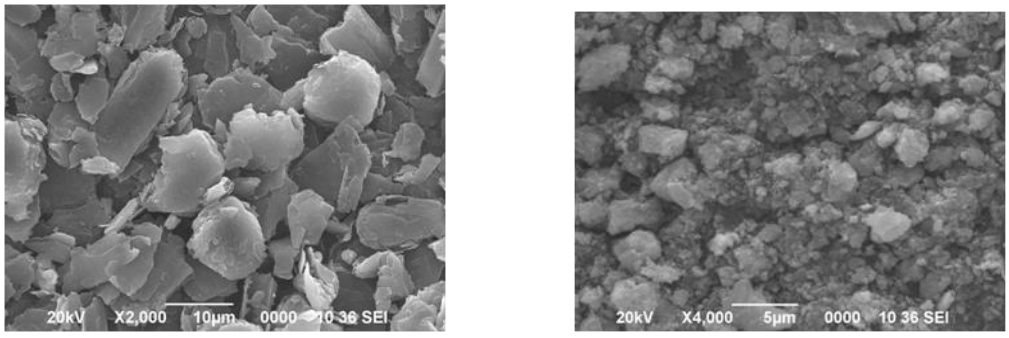

a **b**

Figure 6.3 Scanning Electron Micrographs of (a) Graphite and (b) Fayalite.

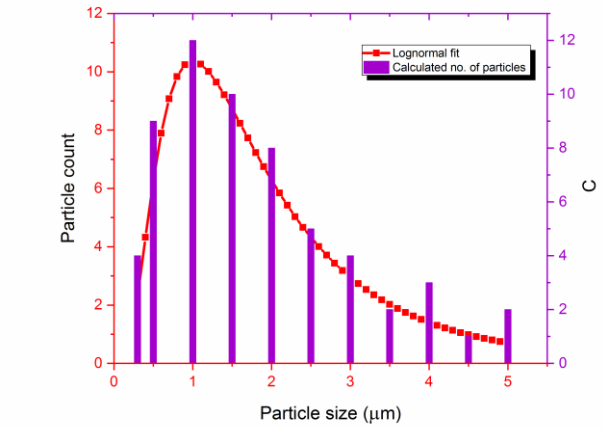

Figure 6.4 Particle size distribution function of the mixture.

The refractive indices of graphite are used as provided by Draine and Lee [34], while for silicates these values are obtained from Fabian et al. [35, 36]. The values are tabulated in Table 6.2.

Table 6.2 Refractive indices of graphite and fayalite

Sample	Wavelength	Real part of refractive index (n)	Imaginary part of refractive index (k)
Graphite	543.5 nm	2.73	1.560
	594.5 nm	2.77	1.593
	632.8 nm	2.80	1.628
Fayalite	543.5 nm	1.844	0.00087
	594.5 nm	1.846	0.00108
	632.8 nm	1.896	0.00144

6.4 Comparative analyses of Model1 and Model2

This sections provides details of the modeling approach and results of DDA computations along with possible explanations. Also the comparative analyses of measured parameters and significance of the models are discussed.

The Percentage elemental composition of graphite and fayalite considered for Model1 and Model2 are provided in Table 6.3.

Table 6.3 Percentage composition of graphite and fayalite particles for Model1 and Model2

Model1	**Graphite (%)**	**Silicate (%)**
	50	50
Model2	10	90
	30	70
	60	40
	90	10

6.4.1 Computational results of Model1

The modeling variables used for Model1 are provided in the Table 6.4.

Table 6.4 Modeling variables of computational Model1

Wavelength	**No. of dipoles**	**No. of scattering directions for $\langle \cos\theta \rangle$**	**No. of orientation directions**
543.5 nm	50k	144148	125
594.5 nm	50k	124985	125
632.8 nm	50k	113121	125

6.4.1.1 The computed parameters

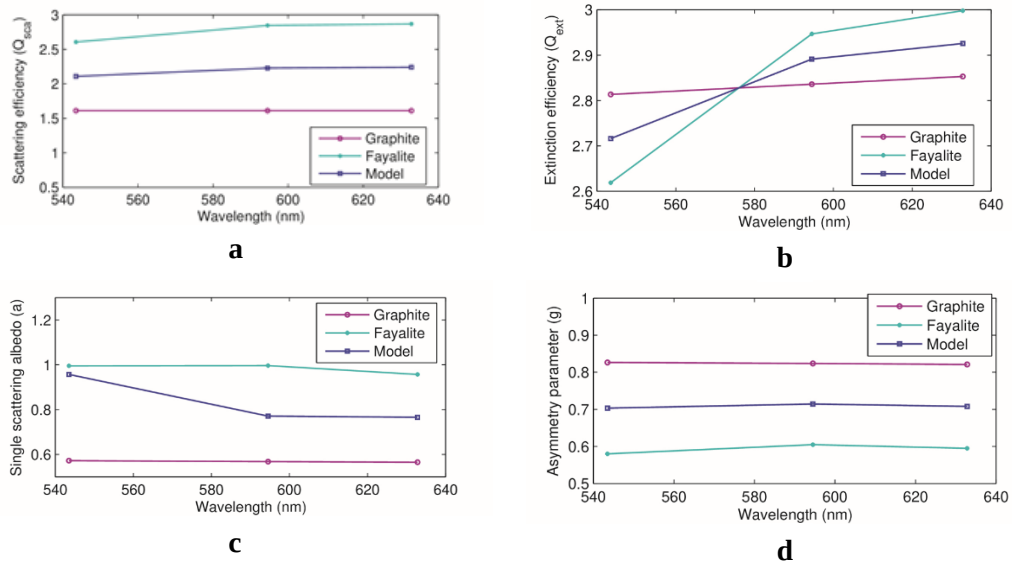

Figure 6.5 The computed values of (a) Scattering efficiency, (b) Extinction efficiency, (c) Single scattering albedo, (d) Asymmetry parameter vs. incident wavelengths for Model1.

The computed values of scattering efficiency (Q_{sca}), extinction efficiency (Q_{ext}), single scattering albedo (a) and asymmetry parameter (g) are shown in Figures 6.5 and 6.6 along with key findings and explanations.

It is observed that the scattering and extinction efficiencies, single scattering albedo values are higher for fayalite while the asymmetry parameter values are lower, than that of graphite (Figure 6.5). The curves follow a similar pattern, with no observable differences in values considering the narrow range of wavelengths. A small difference is seen in the extinction efficiency of fayalite between 543.5 nm and 594.5 nm wavelengths, which resulted in a peculiar curve for the single scattering albedo in the dust model calculations.

6.4.1.2 The comparative analyses for F_{11} and $-F_{12}/F_{11}$

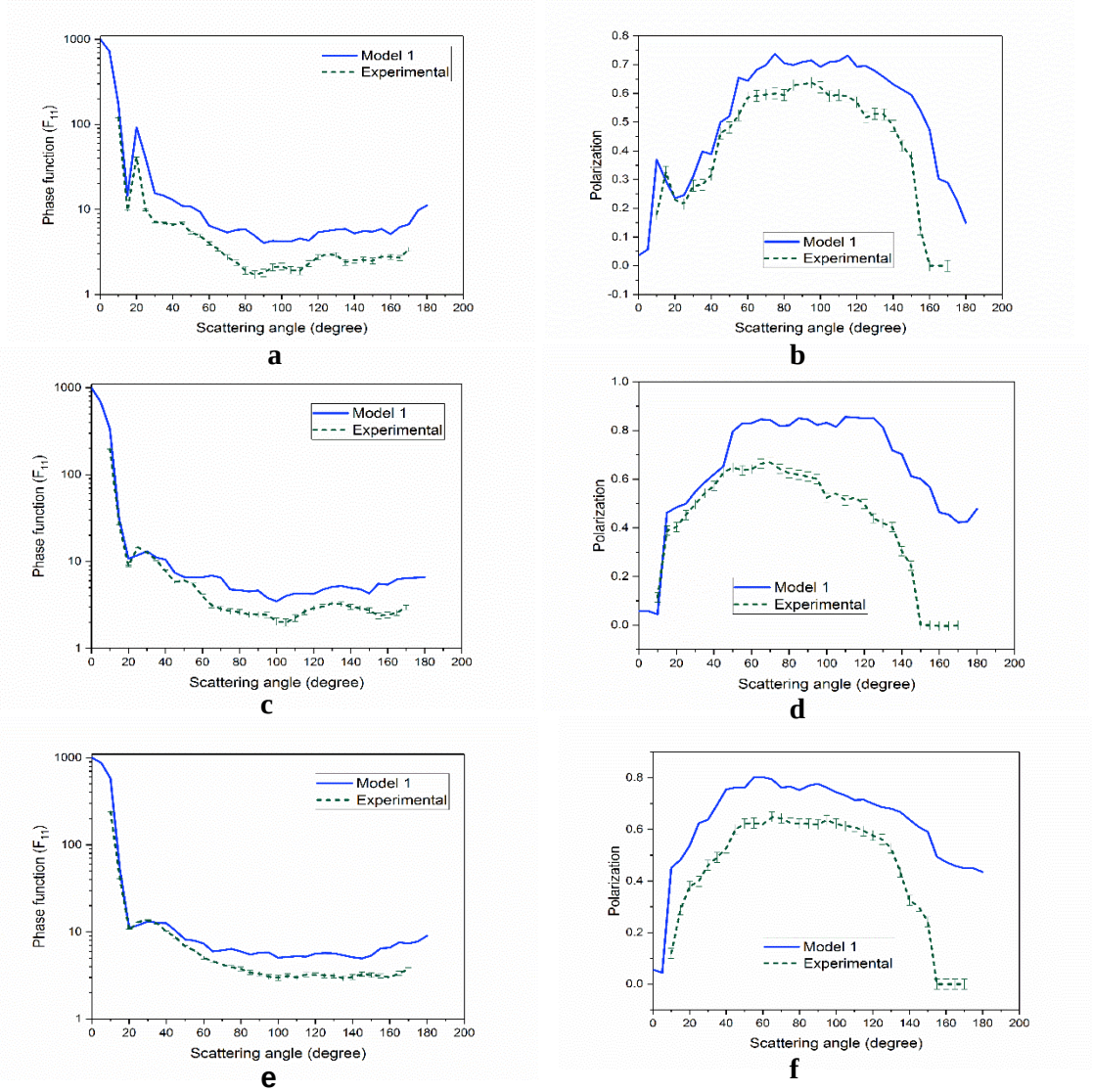

Figure 6.6 Theoretical and experimental phase function and polarization values at incident wavelengths (a) and (b) 543.5 nm, (c) and (d) 594.5 nm and (e) and (f) 632.8 nm respectively for Model1. Experimental curves are plotted with error bars.

The phase functions and polarizations are experimentally measured for a scattering angle range of 10° to 170°. The comparative analyses is done to fit the experimentally measured values. From the plots it is observed that in the computational results are slightly higher than the experimental ones at the three incident wavelengths (Figure 6.6 (a) to (f)). It

may be due to the compositional imbalance between highly absorbing graphite particles as compared to fayalite samples with lower values of imaginary refractive index. The F_{11} values are found to be closer in case of 632.8 nm wavelengths compared to other wavelengths. But $-F_{12}/F_{11}$ is found to be similar for all the wavelengths as revealed by the error analyses. A few negative values of polarization are also observed in the experimental results at higher scattering angles around 140° to 160° at all the wavelengths, not found in the theoretical calculations. While phase function values depends on the characterizing wavelengths and its closeness to the particle sizes, along with the shape averaging. As the incident radiation approaches the particle size, the accuracy and efficiency of the modeling approach becomes reasonable. The dominant parameter influencing the calculated values must be the particle size distribution and its comparability to the incident wavelengths. The number of dipoles considered is an important factor in achieving accuracy and closeness to experimental results. The errors are a combined result of discrepancies in approximating number of orientation directions and compositional assumptions of graphite and silicates. The lesser number of peaks and dips contributing to oscillations in both the theoretical and experimental curve is a result of the extensive shape and size averaging performed to simulate realistic dust.

6.4.2 Computational results Model2

Modeling variables used in Model2 are tabulated in Table 6.5.

Table 6.5 Modeling variables of computational Model2

Wavelength	**No. of dipoles**	**No. of scattering directions for $\langle\cos\theta\rangle$**	**No. of orientation directions**
543.5 nm	100k	144148	180
594.5 nm	100k	124985	180
632.8 nm	100k	113121	180

In the Model2) a few variables are changed to achieve closeness to the experimental results as much as possible considering the theoretical limitations in terms of high computational requirements. The comparative analyses plots are shown in Figure 6.7 and 6.8, along with interpretations and important findings.

6.4.2.1 The computed parameters

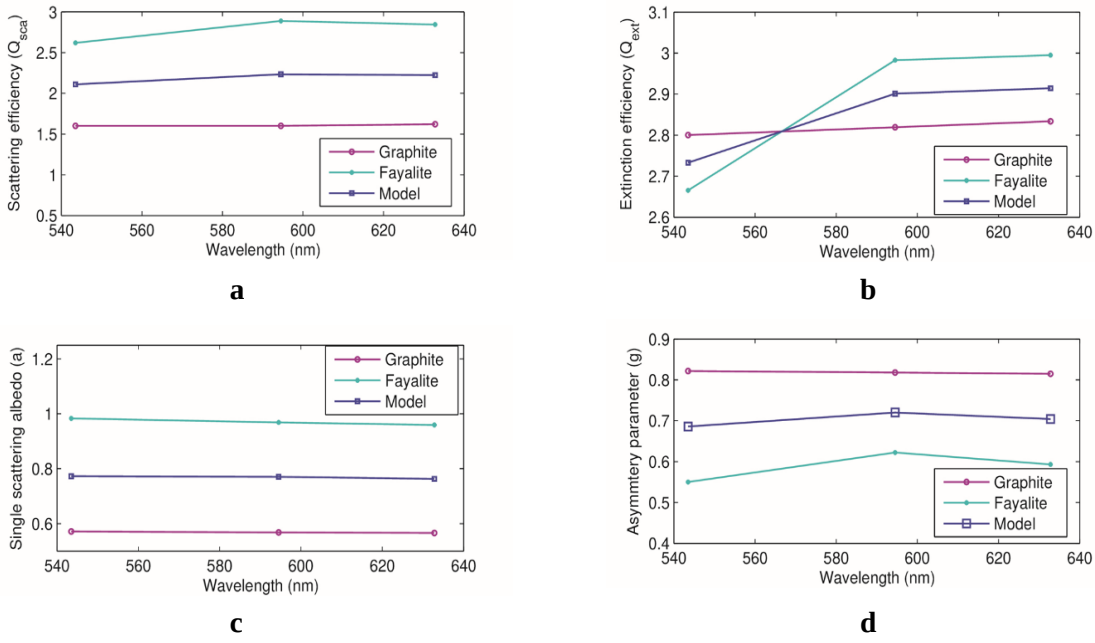

Figure 6.7 The computed values of (a) Scattering efficiency, (b) Extinction efficiency, (c) Single scattering albedo, (d) Asymmetry parameter vs. incident wavelength, for Model 2.

.

The scattering and extinction efficiencies, single scattering albedos shows similar pattern as Model1, with slight changes in the values. But no observable differences between the curves are found other than the small variations in the single scattering albedo. The wavelength range considered is too narrow to differentiate between the computational results of these 4 parameters (Figure 6.7).

Scattering efficiency (Q_{Sca}) vs. size parameter (X) values:

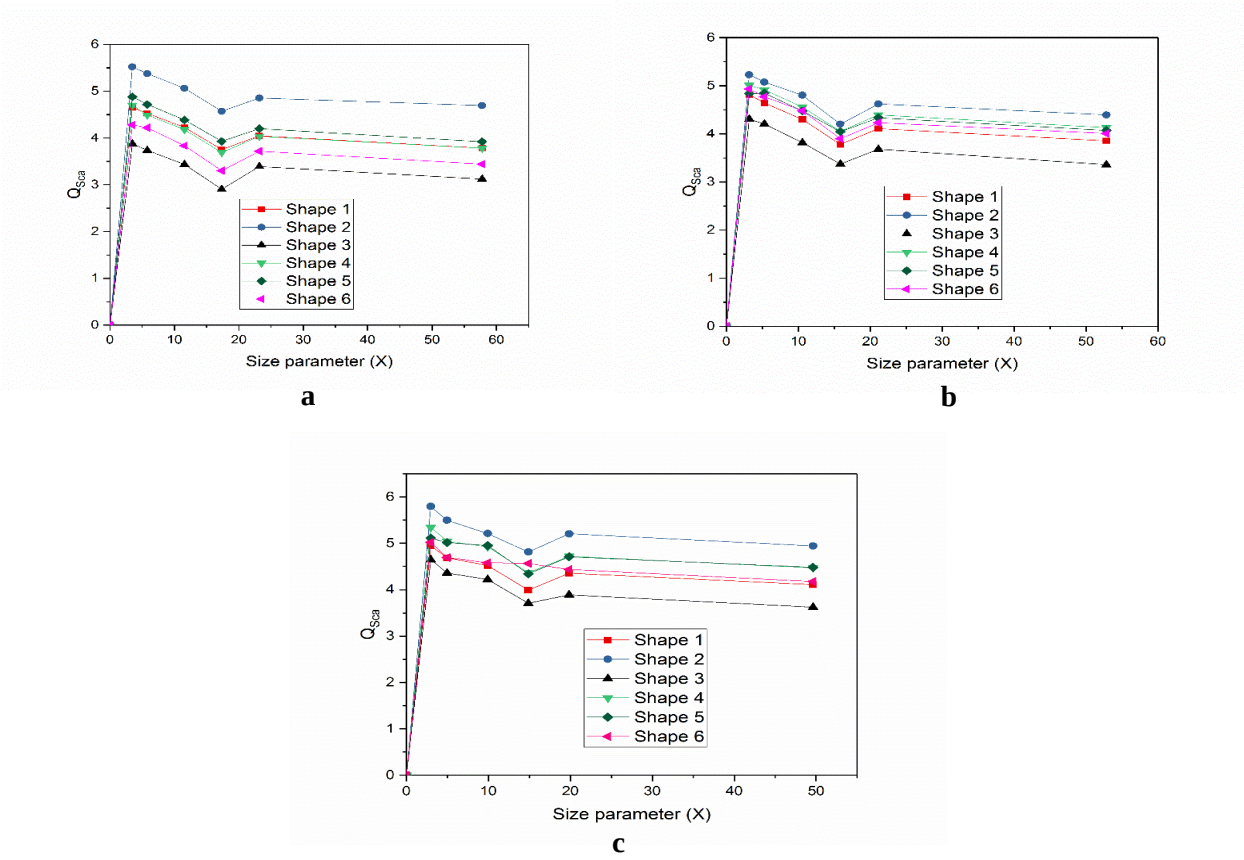

Figure 6.8 Scattering efficiency (Q_{sca}) vs. size parameter at (a) 543.5 nm, (b) 594.5 nm and (c) 632.8 nm wavelengths respectively.

Scattering efficiency **(Q_{Sca})** vs. size parameter (X) value are plotted for the final Model2 at each wavelength for all the six shapes considering the refractive index to be fixed [Figure 6.8]. The Q_{Sca} values are very important to determine the influence of size averaging on the calculated scattering matrix elements [37]. Particularly the shape of these curves are crucial for proper interpretation of the computational results because it is necessary to cut off the calculations at some maximum particle size values to satisfy the $|m|kd$ values and minimize errors. These plots (Figure 6.8 (a), (b) and (c) shows that the major oscillations including the 1st maxima of the curve are concentrated within a typical moderate size parameters range. While the curves are almost flat towards very large size parameters

without any significant features extended upto 5 μm. It is evident that including sizes upto around 2 μm could still provide a quite accurate representation of the laboratory samples. This behavior is almost comparable to a geometric optic regime where all small features of the size distribution are accounted for in the computational curves [37]. Also the strong shape dependence of the size averaged Q_{Sca} curves are evident from the study where each shape produces a distinct pattern for easily distinguishable from the others. But as the wavelength increases the curves move closer to each other with very narrow differences in their values. The aspect ratios also play a vital role in determining the Q_{Sca} values for fixed shapes with the maximum being observed for shape 2 (maximum aspect ratio) and minimum for shape 3. While the near spherical irregular shapes attain closer intermediate values.

6.4.2.2 The comparative analyses for F_{11} and $-F_{12}/F_{11}$

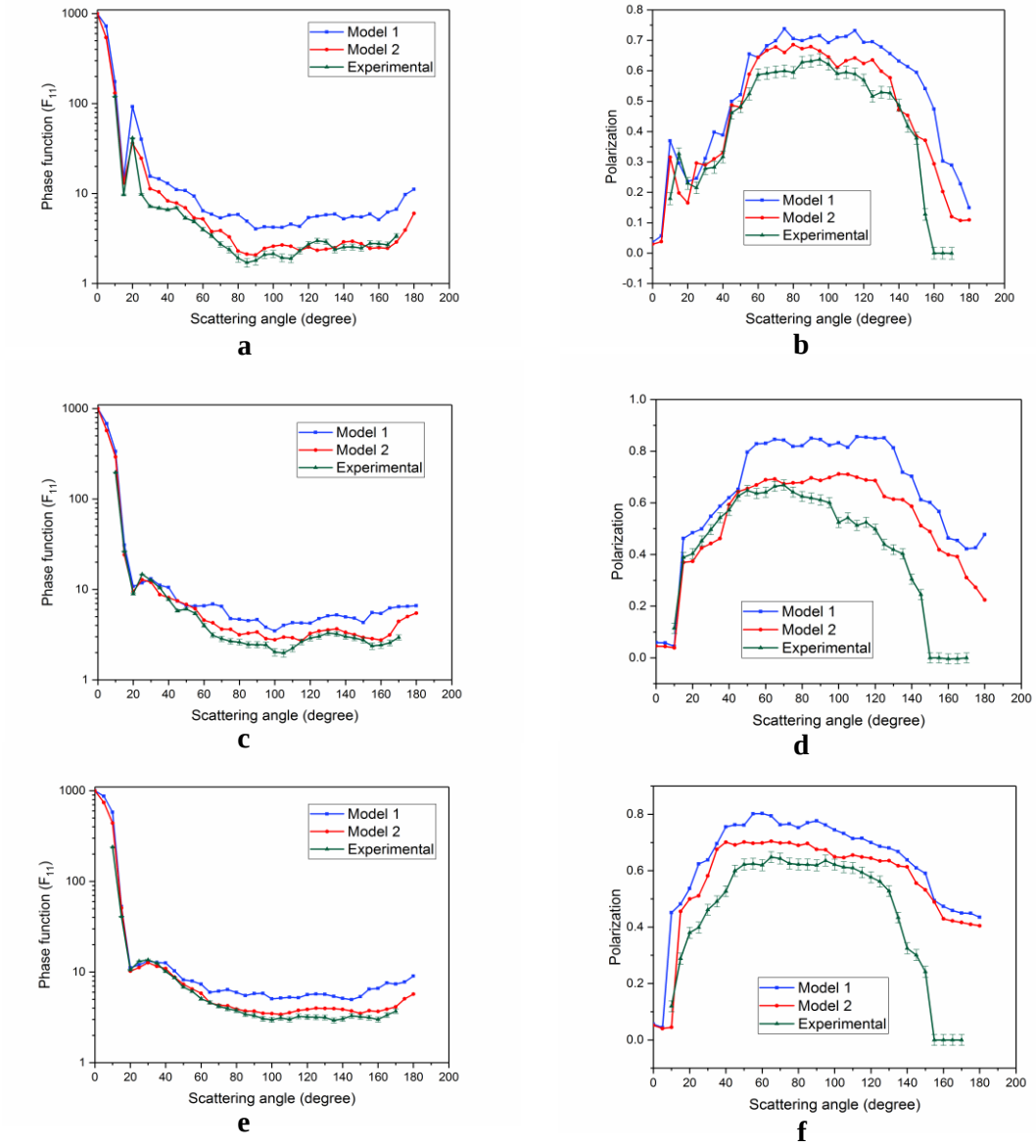

Figure 6.9 Theoretical and experimental phase function and polarization values at incident wavelengths (a) and (b) 543.5 nm, (c) and (d) 594.5 nm and (e) and (f) 632.8 nm respectively for Model2. Experimental curves are plotted with error bars.

Again the size and shape averaged values of scattering parameters are used to reproduce experimental results. Also the values of Model1 are plotted alongside Model2 to observe the changes after modification in the modeling approach. In the second model, the

computational parameters are found to be closer to the averaged values of experimentally measured F_{11} and $-F_{12}/F_{11}$ (Figure 6.8). The rms error values are calculated and averaged over the scattering angle θ for both the models which shows significant reduction of discrepancies between computational and measured values in case of the Model2, provided in the Table 6.6.

Table 6.6 Relative rms errors of Model1 and Model2 as compared with experimental results

Wavelength	**Phase function**		**Polarization**	
	Model1	Model2	Model1	Model2
543.5 nm	4.2384776e+02	1.5463738e+02	2.2192783e-01	1.4746347e-01
594.5 nm	3.9755633e+02	1.4362824e+02	2.1093642e-01	1.2363271e-01
632.8 nm	1.9863392e+02	1.2633091e+02	2.0124316e-01	1.1977673e-01

6.5 Results and Discussions

Model2 efficiently reproduces the experimentally acquired patterns of both the measured scattering parameters F_{11} and $-F_{12}/F_{11}$ with higher accuracy as compared to Model1. The F_{11} curves are found to be of typical shape. While in case of higher scattering angle a few negative values of $-F_{12}/F_{11}$ appears in the experimental results, which are unaccounted for in our model. These unaccounted peaks are previously reported a number of times for cosmic and cometary dust [38-40].

In case of F_{11} the values of Model2 are closer to the experimental results with significant reduction in the calculated rms errors provided in Table 6.6. The increase in the orientation directions has an important effect in smoothing the computational curve making it near identical to the experimental values. The change in composition of the two constituent elements lowers the values of overestimated F_{11} as in Model1. The composition which produces the best results is found out to be the one in which the ratios of graphite and fayalite are 3:2 [Table 6.3]. The increase in number of dipoles directly effects accuracy of the

computation. In case of $-F_{12}/F_{11}$ for Model2, the values still remain closer to those of Model1 but lower values and weaker peaks ensures that it is more comparable to the relatively smoother experimental curves with significant decrease in computational errors.

Shape modeling can be effective for polarization because of its dependence on surface irregularities and sharp edges in the scatterer. At lower scattering angles up to a value of about 25°, the values of theoretical and experimental F_{11} are found to match significantly at all the characterizing wavelengths. But deviations are observed at mid and higher scattering angles upto the maximum measurement angle 170°. A relatively smooth curve is observed for both the parameters in case of 632.8 nm wavelength as compared to 543.5 nm and 594.5 nm. This patterns are typical to irregularly shaped dust particles as observed for computational curves in previous studies [41-42].

The averaging over shapes (considering surface roughness) tends to smooth out the theoretical curves, decreasing the number of small features and oscillations as found in both the theoretical and experimental curves for F_{11} and $-F_{12}/F_{11}$.

These models are not highly accurate but can be considered reliable and efficient in reproducing the observed patterns for scattering parameters of dust mixtures with two or more constituent elements, mainly in the moderate size parameter range.

6.6 Conclusions

1. An interstellar dust analogue model of graphite and fayalite is developed and studied at three incident wavelengths in the visible region. It provides a good approximation to the shape and size distribution of laboratory synthesized realistic dust particles supposed to be present in the interstellar medium.
2. A number of nonconventional modeling variables are used to carry out computational calculations of scattering parameters and their influence on scattering patterns are demonstrated.
3. The modeling approach is effective with the inclusion of additional parameters, provided the number constituent elements are limited (strictly two or three).

References

1. Piovan, L., Tantalo, R., and Chiosi, C. Modelling galaxy spectra in presence of interstellar dust—I. The model of interstellar medium and the library of dusty single stellar populations. *Monthly Notices of the Royal Astronomical Society*, 366(3):923-944, 2006.
2. Siebenmorgen, R., Voshchinnikov, N. V., and Bagnulo, S. Dust in the diffuse interstellar medium-Extinction, emission, linear and circular polarisation. *Astronomy and Astrophysics*, 561:A82, 2014.
3. Draine, B. T. Interstellar dust grains. *Annual Review of Astronomy and Astrophysics*, 41(1):241-289, 2003.
4. Groves, B. A., Dopita, M. A., and Sutherland, R. S. Dusty, radiation pressure-dominated photoionization. I. model description, structure, and grids. *The Astrophysical Journal Supplement Series*, 153(1):9, 2004.
5. Tielens, A. G. G. M. The composition of circumstellar and interstellar dust. In *Tetons 4: Galactic Structure, Stars and the Interstellar Medium*, 231:92, 2001.
6. Krüger, H., Landgraf, M., Altobelli, N., and Grün, E. Interstellar dust in the solar system. *Space Science Reviews*, 130(1-4):401-408, 2007.
7. Altobelli, N., Postberg, F., Fiege, K., Trieloff, M., Kimura, H., Sterken, V.J., Hsu, H.W., Hillier, J., Khawaja, N., Moragas-Klostermeyer, G. and Blum, J. Flux and composition of interstellar dust at Saturn from Cassini's Cosmic Dust Analyzer. *Science*, 352(6283):312-318, 2016.
8. Rotundi, A., Brucato, J. R., Colangeli, L., Ferrini, G., Mennella, V., Palomba, E., and Palumbo, P. Production, processing and characterization techniques for cosmic dust analogues. *Meteoritics and Planetary Science*, 37(11):1623-1635, 2002.
9. Vidali, G., Roser, J. E., Ling, L., Congiu, E., Manicó, G., and Pirronello, V. The formation of interstellar molecules via reactions on dust grain surfaces. *Faraday discussions*, 133:125-135, 2006.

10. Dulieu, F., Congiu, E., Noble, J., Baouche, S., Chaabouni, H., Moudens, A., Minissale, M. and Cazaux, S. How micron-sized dust particles determine the chemistry of our Universe. *Scientific reports*, 3:1338, 2013.
11. Evans, A. C., Meinert, C., Giri, C., Goesmann, F., and Meierhenrich, U. J. Chirality, photochemistry and the detection of amino acids in interstellar ice analogues and comets. *Chemical Society Reviews*, 41(16):5447-5458, 2012.
12. Henning, T., Jäger, C., and Mutschke, H. Laboratory studies of carbonaceous dust analogs. In *Astrophysics of dust*, 309:603, 2004
13. Perets, H.B., Lederhendler, A., Biham, O., Vidali, G., Li, L., Swords, S., Congiu, E., Roser, J., Manicó, G., Brucato, J.R. and Pirronello, V. Molecular hydrogen formation on amorphous silicates under interstellar conditions. *The Astrophysical Journal Letters*, 661(2):L163, 2007.
14. Fraser, H. J., Bisschop, S. E., Pontoppidan, K. M., Tielens, A. G., and Van Dishoeck, E. F. Probing the surfaces of interstellar dust grains: the adsorption of CO at bare grain surfaces. *Monthly Notices of the Royal Astronomical Society*, 356(4):1283-1292, 2005.
15. Gibb, E. L., Whittet, D. C. B., Boogert, A. C. A., and Tielens, A. G. G. M. Interstellar ice: the infrared space observatory legacy. *The Astrophysical Journal Supplement Series*, 151(1):35, 2004.
16. Draine, B. T., and Li, A. Infrared emission from interstellar dust. IV. The silicate-graphite-PAH model in the post-Spitzer era. *The Astrophysical Journal*, 657(2):810, 2007.
17. Messenger, S., Keller, L. P., and Lauretta, D. S. Supernova olivine from cometary dust. *Science*, 309(5735):737-741, 2005.
18. Nieva, M. F., and Przybilla, N. Present-day cosmic abundances-A comprehensive study of nearby early B-type stars and implications for stellar and Galactic evolution and interstellar dust models. *Astronomy and Astrophysics*, 539:A143, 2012.
19. Camps, P., and Baes, M. SKIRT: An advanced dust radiative transfer code with a user-friendly architecture. *Astronomy and Computing*, 9:20-33, 2015.

20. Steinacker, J., Pagani, L., Bacmann, A., and Guieu, S. Direct evidence of dust growth in L183 from mid-infrared light scattering. *Astronomy and Astrophysics*, 511:A9, 2010.
21. Zubko, E., Muinonen, K., Shkuratov, Y., Videen, G., and Nousiainen, T. Scattering of light by roughened Gaussian random particles. *Journal of Quantitative Spectroscopy and Radiative Transfer*, 106(1-3):604-615, 2007.
22. Nousiainen, T., and Muinonen, K. Surface-roughness effects on single-scattering properties of wavelength-scale particles. *Journal of Quantitative Spectroscopy and Radiative Transfer*, 106(1-3):389-397, 2007.
23. Draine, B. T., and Flatau, P. J. Discrete-dipole approximation for scattering calculations. *JOSA A*, 11(4):1491-1499, 1994.
24. Vilaplana, R., Moreno, F., and Molina, A. Study of the sensitivity of size-averaged scattering matrix elements of nonspherical particles to changes in shape, porosity and refractive index. *Journal of Quantitative Spectroscopy and Radiative Transfer*, 100(1-3):415-428, 2006.
25. Mishchenko, M. I., Travis, L. D., and Lacis, A. A. *Multiple scattering of light by particles: radiative transfer and coherent backscattering*. Cambridge University Press, Cambridge, 2006.
26. Mishchenko, M. I. *Electromagnetic scattering by particles and particle groups: an introduction.* Cambridge University Press, Cambridge, 2004.
27. Mishchenko, M. I., and Yurkin, M. A. On the concept of random orientation in far-field electromagnetic scattering by nonspherical particles. *Optics letters*, 42(3):494-497, 2017.
28. Draine, B. T., and Flatau, P. J. User guide for the discrete dipole approximation code DDSCAT 7.3., 2013. *arXiv preprint arXiv:1305.6497*.
29. Nousiainen, T., Zubko, E., Niemi, J. V., Kupiainen, K., Lehtinen, M., Muinonen, K., and Videen, G. Single-scattering modeling of thin, birefringent mineral-dust flakes using the discrete-dipole approximation. *Journal of Geophysical Research: Atmospheres*, 114(D7), 2009.

30. Zubko, E., Muinonen, K., Muñoz, O., Nousiainen, T., Shkuratov, Y., Sun, W., and Videen, G. Light scattering by feldspar particles: comparison of model agglomerate debris particles with laboratory samples. *Journal of Quantitative Spectroscopy and Radiative Transfer*, 131:175-187, 2013.
31. Boruah, M. J., Gogoi, A., Nath, B. C., and Ahmed, G. A. Light scattering studies of randomly oriented polycrystalline fayalite micro particles as interstellar dust analogues. *Journal of Quantitative Spectroscopy and Radiative Transfer*, 196:213-221, 2017.
32. DeAngelis, M. T., Rondinone, A. J., Pawel, M. D., Labotka, T. C., and Anovitz, L. M. Sol-gel synthesis of nanocrystalline fayalite (Fe2SiO4). *American Mineralogist*, 97(4):653-656, 2012.
33. Heintzenberg, J. Properties of the log-normal particle size distribution. *Aerosol Science and Technology*, 21(1):46-48, 1994.
34. Draine, B. T., and Lee, H. M. Optical properties of interstellar graphite and silicate grains. *The Astrophysical Journal*, 285:89-108, 1984.
35. Fabian, D., Henning, T., Jäger, C., Mutschke, H., Dorschner, J. and Wehrhan, O., Steps toward interstellar silicate mineralogy-VI. Dependence of crystalline olivine IR spectra on iron content and particle shape. *Astronomy and Astrophysics*, 378(1):228-238, 2001.
36. Database of Optical Constants for Cosmic Dust, url: http://www.astro.uni-jena.de/Laboratory/OCDB/crsilicates.html
37. Vilaplana, R., Luna, R., and Guirado, D. The shape influence on the overall single scattering properties of a sample in random orientation. *Journal of Quantitative Spectroscopy and Radiative Transfer*, 112(11):1838-1847, 2011
38. Hadamcik, E., Renard, J. B., Levasseur-Regourd, A. C., and Worms, J. C. Polarimetric study of levitating dust aggregates with the PROGRA2 experiment. *Planetary and Space Science*, 50(9):895-901, 2002.
39. Hadamcik, E., Renard, J. B., Rietmeijer, F. J. M., Levasseur-Regourd, A. C., Hill, H. G. M., Karner, J. M., and Nuth, J. A. Light scattering by fluffy Mg–Fe–SiO and C

mixtures as cometary analogs (PROGRA2 experiment). *Icarus*, 190(2):660-671, 2007.

40. Kimura, H., and Mann, I. Light scattering by large clusters of dipoles as an analog for cometary dust aggregates. *Journal of Quantitative Spectroscopy and Radiative Transfer*, 89(1-4):155-164, 2004.
41. Mishchenko, M. I., Travis, L. D., Kahn, R. A., West, R. A. Modeling phase functions for dustlike tropospheric aerosols using a shape mixture of randomly oriented polydisperse spheroids. *Journal of Geophysical Research: Atmospheres*, 102(D14):16831-16847, 1997.
42. Mishchenko, M. I. Electromagnetic scattering by nonspherical particles: A tutorial review. *Journal of Quantitative Spectroscopy and Radiative Transfer*, 110(11):808-832, 2009.